RSC Advances

PAPER

View Article Online
View Journal | View Issue

Cite this: *RSC Adv.*, 2014, **4**, 35383

Study of far infrared optical properties and, photocatalytic activity of ZnO/ZnS hetero-nanocomposite structure

Reza Zamiri,*[a] David Maria Tobaldi,[a] Hossein Abbastabar Ahangar,[b] Avito Rebelo,[a] Maria Paula Seabra,[a] Michael Scott Belsley[c] and J. M. F. Ferreira[a]

Received 4th June 2014
Accepted 22nd July 2014

DOI: 10.1039/c4ra05325g

www.rsc.org/advances

ZnO nanoplates/ZnS nanoparticles as a hetero-nanocomposite structure was prepared by a single pot precipitation method without using any capping ligands or other additives. The morphology of the prepared nanocomposite was studied by scanning electron microscopy (SEM). Optical properties of the prepared samples were studied by UV-visible reflectance and Raman spectroscopy. The FT-IR spectroscopy along with the Kramers Kronig (k k) method and classical dispersion theory were utilized to calculate far-infrared optical constants of the prepared samples. The photocatalytic activity of the prepared nanoheterostructure was also assessed in the gas solid phase, by monitoring the NO_x abatement using a white-lamp to re-create an indoor environment.

I. Introduction

In the past decade, semiconductor nanostructures have attracted much attention due to their size dependent physical and optical properties. As one of the most investigated nanomaterials, ZnO has been widely used in various areas such as optoelectronic devices, lasers, sensors, photocatalysts and photovoltaic devices.[1–6] A remarkable number of reported research works aimed at improving the physical and chemical properties of nanomaterials by surface coating or surface modification as one of the most advanced and intriguing methods.[7] In this context, dramatic changes in optoelectronic properties were observed by surface coating with different band-gap materials.[8] The photocatalytic efficiency of ZnO is not very high due to the rapid recombination of the photogenerated electron–hole pairs in the single phase semiconductor. Therefore, hybrid semiconductor systems are more interesting to promote the separation of electron–hole pairs and retain reduction and oxidation reactions at two different reaction sites.[9] These systems increase the photocatalytic efficiency by suppressing of the recombination of photogenerated electron–hole pairs in semiconductors. So far, many successful efforts have been done on this topic such as SnO_2/ZnO, ZnO/In_2O_3, ZnO/ZnS, and Bi_2O_3/ZnO.[10–13]

It is well known that ZnS is a good photocatalyst because of the rapid generation of electron–hole pairs by photoexcitation and the highly negative reduction potentials of excited electrons. By hybridizing ZnS and ZnO, the recombination rate of the charge carriers significantly decreases due to their physically separated band gap. In addition, the hybrid structure ZnO/ZnS showed the lower photo-excitation threshold energy compared to the individual component.

The ZnO/ZnS binary heterostructures with different morphologies, such as biaxial nanowires,[12] nanorings,[14] hollow nanocages, and saw-like nanostructures, have also been synthesized *via* solution-based chemical routes.[12,14,15] The main disadvantages of these fabrication methods are the necessary vacuum conditions, and the use of high temperature or surface active agents, which lead to increasing impurities in final products.

In this paper, we report a facile and simple approach to synthesize ZnO nanoplates/ZnS nanoparticles by a single one-pot template free precipitation route without need for any capping ligands or other additives. The optical and dielectric properties of the prepared ZnO/ZnS nanocomposite were also studied in the far-infrared regime. In addition, the photocatalytic properties were studied in detail and, for the first time in that system, accounting for the NO_x abatement in gas–solid phase, using a white-light lamp (simulating an artificial indoor lightning). These pollutants are responsible for different problems such as tropospheric ozone, ozone layer depletion, photochemical smog, acid rain, and even global warming caused by NO_x.[16]

The results indicate that the as prepared products exhibit better photocatalytic activity (PCA) than single phase ZnO nanostructure toward the decomposition of NO_x using a white-lamp irradiation.

[a]*Department of Materials and Ceramic Engineering (DEMaC), CICECO, University of Aveiro, Campus Santiago, 3810 193 Aveiro, Portugal. E mail: zamiri.r@gmail.com*
[b]*Faculty of Chemistry, Kharazmi (TarbiatMoallem) University, Tehran, Iran*
[c]*CFUM, Department of physics, University of Minho, 4710 059, Braga, Portugal*

II. Experimental

ZnO nanoplates/ZnS nanoparticles were prepared by a wet chemical precipitation method. Firstly, 3.352 g (24.6 mmol) of $ZnCl_2$ (Aldrich, Germany) was dissolved in distilled water. Then, the obtained solution was added dropwise into100 mL of 0.1 M NaOH (Merck, Germany) solution. The pH value of the resulting solution was around 13. Subsequently, 38 mmol Na_2S was added slowly to the mixture and the resulting suspension was kept at room temperature for 2 h under mild magnetic stirring to yield the hetero structures. Then, the dark yellow product was washed with distilled water for several times and collected by centrifuging. Finally, the as-prepared and collected product was dried at 80 °C for 3 h. The chemical reactions are as follows:

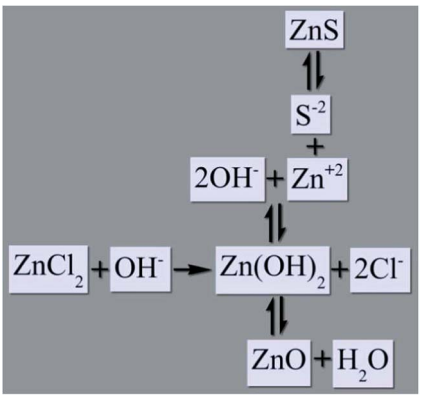

For comparison purposes, the ZnO nanoplates were also prepared by the same process, but without using Na_2S reagent. The structure, morphology and chemical analysis of the samples were studied by X-ray diffraction (Shimadzu XRD-6000, Tokyo, Japan), Scanning Electron Microscopy (SEM, SU-70, Hitachi) and energy-dispersive X-ray spectroscopy (EDS). The study of the optical properties of the samples was carried out by diffuse reflectance spectroscopy (DRS) (Perkin-Elmer, Lambda 35), spectra of the samples were acquired in the UV-Vis range (250–750 nm), with 0.2 nm step-size and using an integrating sphere and a white reference material, both made of $BaSO_4$. With the aim of converting the diffuse reflectance into the absorption coefficient α, the Kubelka–Munk function was applied:[17]

$$\alpha \approx \frac{K}{S} = \frac{(1 - R_\infty)^2}{2R_\infty} \equiv F(R_\infty) \quad (1)$$

where K and S are the absorption and scattering coefficients; the reflectance R_∞ is equal to $R_{sample}/R_{standard}$.

Also Raman (laser wavelength 1064 nm; laser power 350 mW) and FTIR (Bruker RFS/100) spectrometry were used. PCA tests of the prepared samples were also assessed. Tests were made in gas–solid phase, monitoring the degradation of NO_x ($NO + NO_2$). The reactor used at this purpose, has been previously described in detail.[18] It consists of a stainless steel cylinder (35 L in volume), and operated under continuous conditions. A white lamp (artificial indoor light), irradiating only in the visible region (Philips LED Bulb Warm white), was used as the light source. This was placed 28 cm from the photocatalyst, so as to have a light intensity – measured by way of a radiometer (Delta OHM, HD2302.0, Italy) – reaching it of approximately 7 W m^{-2} in the visible range, whilst being zero in the UVA. Samples were prepared in the form of a thin layer of powder, with a constant mass (0.10 g), and thus approximately constant thickness, in a 6 cm diameter Petri dish. The tests were performed at room temperature – 27 ± 1 °C (temperature inside the reactor), with a relative humidity of 31%. These parameters (temperature and relative humidity), remained stable all over the tests, and were controlled, respectively, by way of a thermocouple placed inside the chamber, and a humidity sensor placed in the inlet pipe. The outlet concentration of the pollutant gas was measured using a chemiluminescence analyzer (AC-30 M, Environment SA, FR). After having placed the photocatalyst inside the reactor, and covered the glass window, the inlet gas mixture (prepared using synthetic air and NO_x gas) was allowed to start flowing until it stabilized at a concentration of 0.2 ppm.[19] Two mass flow controllers were used to prepare such a mixture of air with this concentration of NO_x. Once the desired concentration was reached, the window glass was uncovered, the lamp turned on, and the PCA reaction started. Photocatalytic tests were assessed for a total irradiation time of 20 min, and they were performed in triplicate, aiming at verifying the stability of the photocatalysts.

III. Result and discussions

Fig. 1 presents the XRD patterns of the nanostructured ZnO and ZnO/ZnS nanocomposite. In the case of ZnO all the diffraction peaks are well indexed to hexagonal wurtzite ZnO structure (JCPDS file no. 36-1451), indicating that the as prepared nanostructured ZnO is crystalline and of high purity.[7,20] However, when synthesis was carried out in the presence of Na_2S, the intensity of the diffraction peaks decreased significantly and new ones belonging to the cubic sphalerite ZnS (JCPDS file no. 05-0566) appeared in the ZnO/ZnS nanocomposite sample. For the ZnO/ZnS nanocomposite, the diffraction peaks of ZnS indexed to (220) and (311) overlap with the (102) and (110) diffraction peaks of the ZnO. Since the proportion of ZnO in the sample is reduced, the intensity of ZnO diffraction peaks was also reduced.

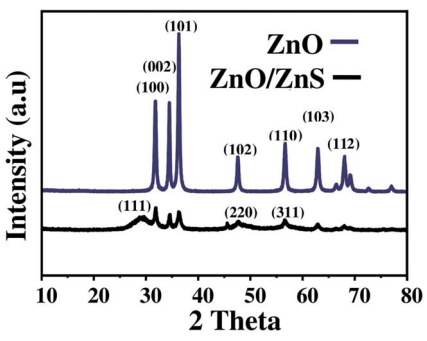

Fig. 1 The XRD patterns of ZnO nanostructure and ZnO/ZnS nanocomposite.

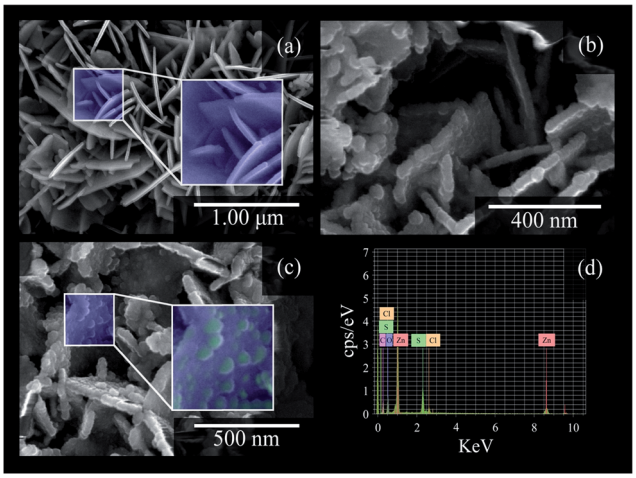

Fig. 2 The SEM images of (a) ZnO nanoplates, (b and c) ZnO/ZnS nanocompositeand (d) EDS analysis of ZnO/ZnS nanocomposite.

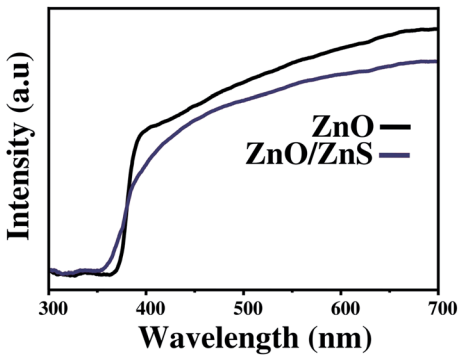

Fig. 3 UV-visible reflectance spectra of ZnO nanostructure and ZnO/ZnS nanocomposite.

The morphological features of the as prepared samples were observed by SEM and the micrographs are presented in Fig. 2. It can be seen that the ZnO nanoparticles exhibit a plate like shape with relatively smooth surfaces (Fig. 2a). Although the overall plate like morphology seems to prevail also for ZnO/ZnS nanocomposite particles, their surfaces appear much rougher (Fig. 2b and c). The approximate composition of the ZnO/ZnS nanocomposite sample was assessed by EDS analysis. The obtained results shown in Fig. 2d confirm the presence of Zn, S and O in the final product. The absence of extra peaks, besides the expectable ones, suggests that the obtained material is of high purity.

Fig. 3 shows the UV-visible reflectance spectra of nanostructured ZnO and ZnO/ZnS nanocomposite. The characteristic absorption band of nanostructured ZnO due to the metal–ligand charge transfer (MLCT) appeared at around 370 nm, while a blue shift on the absorption spectrum is observed in the case of ZnO/ZnS nanocomposite. This is because of the characteristic absorption band of ZnS nanoparticles is located between 220–350 nm.[21]

The wurtzite structure of ZnO belongs to the $^4C_{6v}$ space group, with 4 atoms per each unit cell. The following modes can be predicted for optical modes according to group theory:

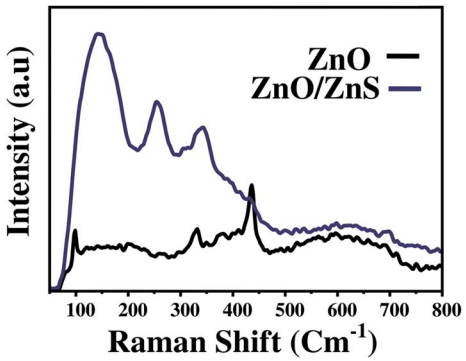

Fig. 4 Raman spectra of ZnO nanoplate and ZnO/ZnS nanocomposite.

$$\Gamma = A1 + 2B1 + E1 + 2E2$$

Among these phonons, A1 + E1 + 2E2 modes are Raman active, A1 and E1 are infrared active, while B1 (low) and B1 (high) modes are normally silent. A1 and E1 branches split into transverse optical (TO) and longitudinal optical (LO) components due to their polar symmetry. The Raman spectra of ZnO nanoplates and of ZnO/ZnS nanocomposite sample are displayed in Fig. 4. According to the literature, [22] the peaks at 334 cm^{-1}, 438 cm^{-1} and 580 cm^{-1} can be attributed to A1 (TO), E2 (high) and A1 (LO), respectively.[22–24] No remarkable shifts could be observed for the 334 cm^{-1} and 434 cm^{-1} peaks of ZnO/ZnS nanocomposite, while the intensities of the peaks were greatly decreased in comparison to those of ZnO nanoplates (Fig. 4). On the other hand, the LO phonon peak of ZnS nanoparticle was observed at 345 cm^{-1} while the TO phonon was observed at 262 cm^{-1}. The first-order LO and TO phonons of ZnS nanoparticles reveals a shift towards the lower energy compared to the Raman spectrum of bulk hexagonal ZnS (TO: 274 cm^{-1} and LO: 352 cm^{-1}). In addition, other Raman peaks at 145 cm^{-1}, 175 cm^{-1}, 386 cm^{-1}, and 440 cm^{-1} are also observed.

The FT-IR spectra of the samples are shown in Fig. 5. The characteristic ZnO absorption band was observed at around 407 cm^{-1}. It is clear that the intensity of this peak decreased for the

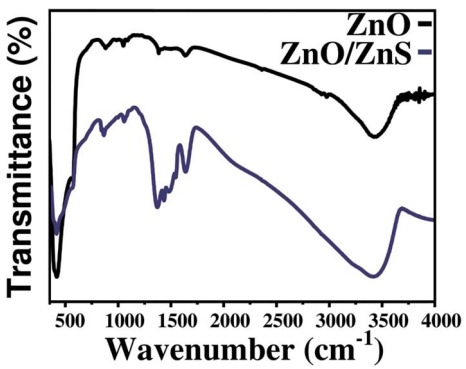

Fig. 5 FT-IR spectra of ZnO nanostructure and ZnO/ZnS nanocomposite.

ZnO/ZnS nanocomposite particles. The broad and small peaks located at 3400 cm^{-1} and 1600 cm^{-1} can be attributed to the stretching and bending vibrations of the O–H bond of the adsorbed H_2O molecules on the surface of ZnO. The intensity of the peaks at around 3400 cm^{-1} and 1600 cm^{-1} increased, indicating a higher density of O–H groups adsorbed onto the surface of ZnO/ZnS nanocomposite,[7,25] in good consistency with its more disordered structure in comparison to pure ZnO nanoplates.

The K–K method along with FT-IR reflectance (R) spectra were used to obtained the Far-inferred optical constants of the prepared ZnO nanoplate and ZnO/ZnS nanocomposite. The refractive index n is an important physical parameter in optical design and generally is a complex quantity as following:

$$\tilde{n}(\omega) = n(\omega) + ik(\omega) \quad (2)$$

where $n(\omega)$ and $k(\omega)$ are the real and the imaginary parts of the complex refractive index respectively, and can be obtained by the following equations:[26]

$$n(\omega) = \frac{1 \quad R(\omega)}{1 + R(\omega) \quad 2\sqrt{R(\omega)}\cos\varphi(\omega)} \quad (3)$$

$$k(\omega) = \frac{2\sqrt{R(\omega)}\cos(\varphi)}{1 + R(\omega) \quad 2\sqrt{R(\omega)}\cos b \quad \varphi(\omega)} \quad (4)$$

Here, $\varphi(\omega)$ is the phase change between the incident and the reflected signals at a particular wavenumber and $R(\omega)$ is the reflectance at particular wave number. This phase change can be calculated from the K–K dispersion relation:[26]

$$\varphi(\omega) = \frac{\omega}{\pi}\int_0^{\infty} \frac{\ln R(\omega') \quad \ln R(\omega)}{\omega'^2 \quad \omega^2} d\omega' \quad (5)$$

This integral can be precisely evaluated by Maclaurin's method:[27]

$$\varphi(\omega_j) = \frac{4\omega_j}{\pi} \times \Delta\omega \times \sum_i \frac{\ln\left(\sqrt{R(\omega)}\right)}{\omega_i^2 \quad \omega_j^2} \quad (6)$$

where $\Delta\omega = \omega_{j+1} \quad \omega_j$. If j is an even number then $i = 1, 3, 5, 6, \ldots j \quad 1, j + 1 \ldots$, while, if j is an odd number then $i = 2, 4, 6, \ldots j \quad 1, j + 1, \ldots$.

In addition, the dielectric function can be obtained by the square of the refractive index. Therefore, the real and imaginary parts of the complex dielectric function are as following:

$$\begin{aligned} &\bar{\varepsilon} = [\tilde{n}(\omega)]^2 = [n(\omega) + ik(\omega)]^2 \\ &\Rightarrow \varepsilon' + i\varepsilon'' = n^2(\omega) \quad k^2(\omega) + 2in(\omega)k(\omega) \\ &\Rightarrow \begin{cases} \varepsilon'(\omega) = n^2(\omega) \quad k^2(\omega) \\ \varepsilon''(\omega) = 2n(\omega)k(\omega) \end{cases} \end{aligned} \quad (7)$$

The far infrared optical constants of the ZnO nanoplate and ZnO/ZnS nanocomposite were calculated and the obtained spectrums are presented in Fig. 6a–d.

The TO and LO optical phonons are useful parameters to illustrate the optical interactions of light with the lattice. The LO mode frequencies are obtained from the imaginary part of

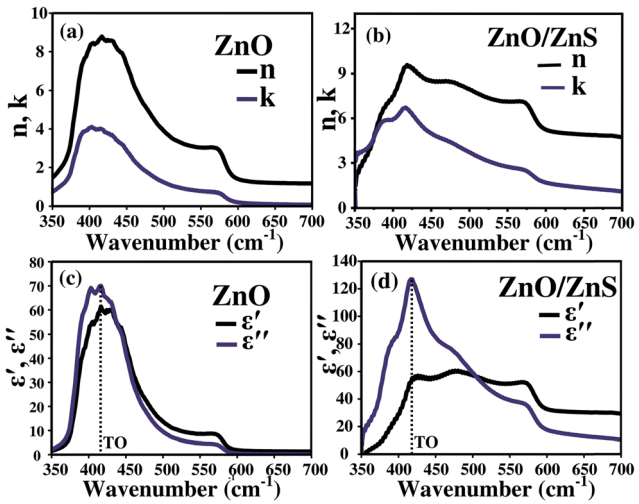

Fig. 6 (a and b) refractive index and extinction coefficient, (c and d) real and imaginary parts of dielectric functions of ZnO nanoplate and ZnO/ZnS nanocomposite.

$1/\varepsilon$ (Fig. 7a and b) and TO mode frequencies correspond to the peaks of the imaginary part of the dielectric function, as indicated in Fig. 7a and b.[28] The obtained values of transverse and longitudinal optical phonons of ZnO nanoplate and ZnO/ZnS nanocomposite are listed in Table 1.

The results of PCA are shown in Table 2, where are reported the pseudo-first order kinetic constants after the first run; in Fig. 8 are depicted the PCA results, repeated in triplicate, of the ZnO/ZnS nanocomposites.

As can be seen in Table 2, ZnO had a negligible PCA under white-light irradiation. This is not surprising, as its E_g lies in the UVA region (see Fig. 3). On the contrary, ZnO/ZnS nanocomposite, had a PCA 3.5 times higher, under the same experimental conditions.

The reaction path for NO_x conversion is mediated by $OH^{\bullet}$ radicals: the O_2^- and $OH^{\bullet}$ radicals formed during photocatalysis react with the pollutant gas, resulting in the production of HNO_3:[29]

$$ZnO/ZnS + h\nu \rightarrow e_{CB}^- + h_{VB}^+ \quad (8)$$

$$h_{VB}^+ + H_2O_{(ads)} \rightarrow OH^{\bullet} + H^+ \quad (9)$$

$$h_{VB}^+ + OH^- \rightarrow OH^{\bullet} \quad (10)$$

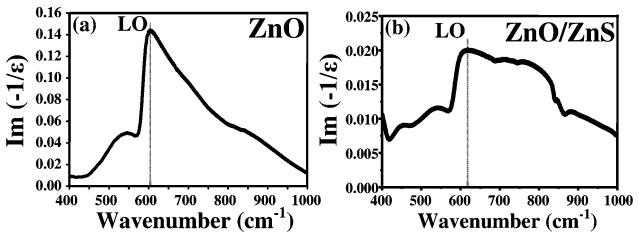

Fig. 7 Imaginary part of $1/\varepsilon$ for ZnO nanostructure and ZnO/ZnS nanocomposite.

Table 1 Optical phonons of ZnO nanostructure and ZnO/ZnS nanocomposite

Material	Transfer optical phonon (TO), cm ^{1}	Longitude optical phonon (LO), cm ^{1}
ZnO	415	604
ZnO/ZnS	418	620

Table 2 Pseudo-first order kinetic constants, and relative correlation coefficients for the tested samples, in case of NO_x degradation in gas solid phase, using the white indoor lamp

Material	$k_{20} \times 10^2$ (min ^{1})	R^2
ZnO	0.075 ± 0.010	0.963
ZnO/ZnS	0.266 ± 0.012	0.996

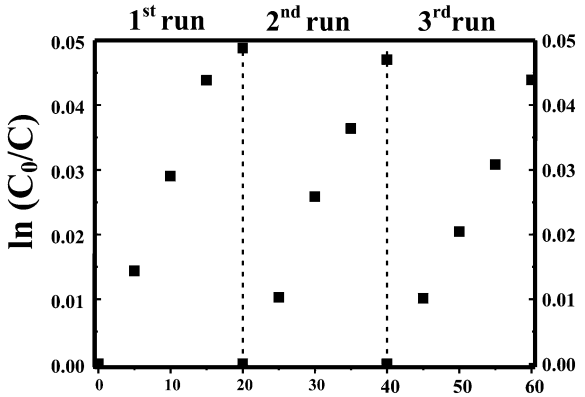

Fig. 8 Photocatalitic activity results, repeated in triplicate, of the ZnO/ZnS nanocomposites.

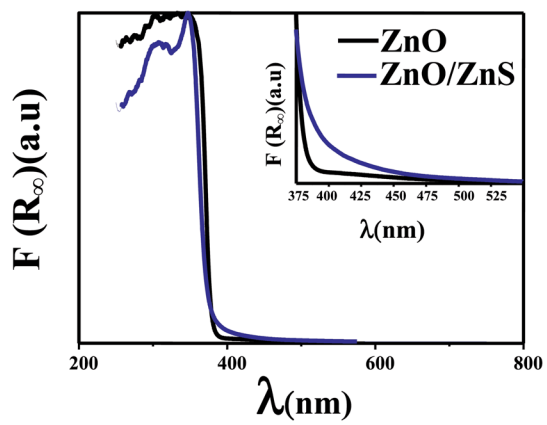

Fig. 9 Kubelka Munk elaboration of the reflectance spectra reported in Fig. 3; in the inset is shown a magnification, in the lambda range 375 550 nm, in order to emphasize the absorption tail into the visible region of the ZnO/ZnS nanocomposite.

$$e_{CB}^{-} + O_2 \rightarrow O_2^{\bullet -} \quad (11)$$

$$NO + OH^{\bullet} \rightarrow NO_2 + H^{+} \quad (12)$$

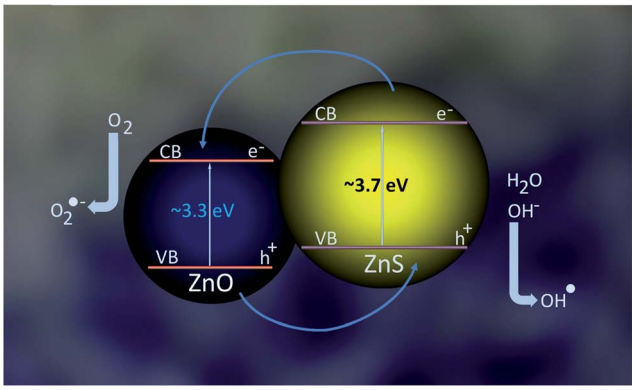

Fig. 10 Simplified schematic diagram of energy band structure and electron hole separation in the ZnO/ZnS nanocomposite.

$$NO + O_2^{\bullet -} \rightarrow NO_3^{-} \quad (13)$$

$$NO_2 + OH^{\bullet} \rightarrow NO_3^{-} + H^{+} \rightarrow HNO_3 \quad (14)$$

Moreover, the HNO_3 produced on the surface of the catalyst, might act as a physical barrier, hence, it might inhibit the photocatalytic reaction.[30]For this reason, with the aim of verifying the stability of the photocatalyst, tests were repeated in triplicate. In Fig. 8 are shown the recycling tests of ZnO/ZnS nanocomposites – ZnO nanoplate showed no PCA after the weak activity of the first run (data not reported here). It is seen that under identical conditions, and after three runs, no significant change in the PCA happened. Therefore, we can reckon that ZnO/ZnS nanocomposites underwent no dissolution after those recycling PCA tests that are repeatable.

The ZnS nanoparticles distributed all over the surface of the ZnO/ZnS nanocomposite, as observed by SEM investigations (Fig. 2b and c), could not only become trapping sites for the photo-generated electrons (thus helping the electron–hole separation),[31] but they are also able to slightly extend the absorption in the visible-region – as depicted in inset of Fig. 9 due to electronic interaction between ZnO and ZnS.[32]

Moreover, as the conduction band of ZnS lies at a more negative potential, compared to that of ZnO, whilst the valence band of ZnO is more positive than that of ZnS (Fig. 10),[33] when the ZnO/ZnS nanocomposites are exposed to visible-light irradiation, the photo-generated electrons are able to migrate from the conduction band of ZnS to that of ZnO and, in the same time, a hole transfer happens from the valence band of ZnO to that of ZnS.[34] Also, the higher density of O–H groups that are adsorbed onto the surface of ZnO/ZnS nanocomposite (compared to ZnO), plays a significant role in the photocatalytic reaction: they enhance the PCA, generating chemical oxidative species, such as hydroxyl radicals, that "switch on" the photocatalytic oxidation of NO_x.[35]

IV. Conclusion

Single phase ZnO nanoplates and biphasic ZnO/ZnS nanoparticles were successfully prepared by a simple and low cost

chemical precipitation technique as confirmed by the obtained XRD analysis. The structural disturbance caused by the anionic size mismatch between oxygen and sulfur resulted in significant morphological changes as seen in the SEM micrographs. The optical properties of the prepared samples, under UV-visible reflectance and Raman spectroscopy, were also significantly affected by the presence of ZnS nanoparticles. The refractive index and dielectric constants of the samples were calculated in far infrared regime using FT-IR spectroscopy and K–K method. The evaluation of optical constants of ZnO based hetrostructures is of considerable importance for applications in integrated optic devices such as switches, filters and optical testers, *etc.*, where the refractive index of a material is the key parameter for device design. The values of TO and LO phonon modes were also calculated and the amounts are 418 cm^{-1} and 620 cm^{-1} respectively. Moreover, the prepared ZnO/ZnS nanocomposite showed itself to be photocatalytically active in the NO_x abatement under visible light (artificial indoor lighting) exposure.

Acknowledgements

The author Reza Zamiri, would like to express his personal thanks to FCT (Fundação para a Ciência e a Tecnologia) for post-doctoral research grant with reference numbers (SFRH/BPD/76185/2011). David M.Tobaldi is grateful to the ECO-SEE project (European Union's Seventh Framework Programme funding, grant agreement no 609234). Note: The views expressed are purely those of the authors and may not in any circumstances be regarded as stating an official position of the European Commission. The support from CICECO is also acknowledged.

References

1 X.-L. Yu, *et al.*, Synthesis and sensing properties of ZnO/ZnS nanocages, *Nanoscale Res. Lett.*, 2010, **5**(3), 644–648.
2 P. Lu and D. Xue, Selective synthesis of ZnO arrays, *Surf. Rev. Lett.*, 2010, **17**(02), 261–264.
3 R. Zamiri, *et al.*, Er doped ZnO nanoplates: Synthesis, optical and dielectric properties, Part B, *Ceram. Int.*, 2014, **40**(1), 1635–1639.
4 R. Zamiri, *et al.*, Laser assisted fabrication of ZnO/Ag and ZnO/Au core/shell nanocomposites, *Appl. Phys. A: Mater. Sci. Process.*, 2013, 1–7.
5 R. Zamiri, *et al.*, Aqueous starch as a stabilizer in zinc oxide nanoparticle synthesis *via* laser ablation, *J. Alloys Compd.*, 2012, **516**, 41–48.
6 R. Zamiri, *et al.*, Electrical properties of Ag-doped ZnO nanoplates synthesized *via* wet chemical precipitation method, *Ceram. Int.*, 2014, **40**(3), 4471–4477.
7 D. Wu, *et al.*, ZnO–ZnS heterostructures with enhanced optical and photocatalytic properties, *J. Nanopart. Res.*, 2011, **13**(7), 2875–2886.
8 B. Tang, *et al.*, Synthesis and optical properties of vertically aligned ZnO nanorods, *J. Nanosci. Nanotechnol.*, 2010, **10**(3), 1842–1845.
9 W. Jia, *et al.*, Towards a highly efficient simulated sunlight driven photocatalyst: a case of heterostructured ZnO/ZnS hybrid structure, *Dalton Trans.*, 2013, **42**(39), 14178–14187.
10 L. Zheng, *et al.*, Network structured SnO2/ZnO heterojunction nanocatalyst with high photocatalytic activity, *Inorg. Chem.*, 2009, **48**(5), 1819–1825.
11 Z. Wang, *et al.*, Highly photocatalytic ZnO/In_2O_3 heteronanostructures synthesized by a coprecipitation method, *J. Phys. Chem. C*, 2009, **113**(11), 4612–4617.
12 X. Wu, *et al.*, Mismatch strain induced formation of ZnO/ZnS heterostructured rings, *Adv. Mater.*, 2007, **19**(17), 2319–2323.
13 S. Balachandran and M. Swaminathan, The simple, template free synthesis of a Bi_2S_3–ZnO heterostructure and its superior photocatalytic activity under UV-A light, *Dalton Trans.*, 2013, **42**(15), 5338–5347.
14 J. Yan, *et al.*, Structure and cathodoluminescence of individual ZnS/ZnO biaxial nanobelt heterostructures, *Nano Lett.*, 2008, **8**(9), 2794–2799.
15 G. Shen, D. Chen and C. J. Lee, Hierarchical saw-like ZnO nanobelt/ZnS nanowire heterostructures induced by polar surfaces, *J. Phys. Chem. B*, 2006, **110**(32), 15689–15693.
16 K. Skalska, J. S. Miller and S. Ledakowicz, Trends in NO x abatement: A review, *Sci. Total Environ.*, 2010, **408**(19), 3976–3989.
17 A. S. Marfunin, *Physics of Minerals and Inorganic Materials: An Introduction*, Springer, Berlin, First edn, 1979, ISBN: 0387089829.
18 D. M. Tobaldi, *et al.*, Ag-Modified Nano-Titania as an Antibacterial Agent and Photocatalyst, *J. Phys. Chem. C*, 2014, **118**, 4751–4766.
19 A. Lawrence, A. Masih and A. Taneja, Indoor/outdoor relationships of carbon monoxide and oxides of nitrogen in domestic homes with roadside, urban and rural locations in a central Indian region, *Indoor Air*, 2005, **15**(2), 76–82.
20 R. Zamiri, *et al.*, Effects of rare-earth (Er, La and Yb) doping on morphology and structure properties of ZnO nanostructures prepared by wet chemical method, Part A, *Ceram. Int.*, 2014, **40**(1), 523–529.
21 P. Scherrer, *Bestimmung der Grösse und der inneren Struktur von Kolloidteilchen mittels Röntgenstrahlen*, Nachrichten von der Gesellschaft der Wissenschaften zu Göttingen, mathematisch-physikalische Klasse, 1918. 1918, p. 98–100.
22 M. Rajalakshmi, *et al.*, Optical phonon confinement in zinc oxide nanoparticles, *J. Appl. Phys.*, 2000, **87**(5), 2445–2448.
23 M. Abdulkhadar and B. Thomas, Study of Raman spectra of nanoparticles of CdS and ZnS, *Nanostruct. Mater.*, 1995, **5**(3), 289–298.
24 S. Scholz, *et al.*, Nanoporous aggregates of ZnS nanocrystallites, *Appl. Organomet. Chem.*, 1998, **12**(5), 327–335.
25 M. A. Vergés, A. Mifsud and C. Serna, Formation of rod-like zinc oxide microcrystals in homogeneous solutions. Journal of the Chemical Society, *Faraday Trans.*, 1990, **86**(6), 959–963.
26 V. Lucarini, *et al.*, *Kramers-Kronig Relations in Optical Materials Research*, Springer Series in Optical Sciences, 2005.

27 M. Ghasemifard, S. Hosseini and G. H. Khorrami, Synthesis and structure of PMN–PT ceramic nanopowder free from pyrochlore phase, *Ceram. Int.*, 2009, **35**(7), 2899–2905.
28 S. Ng, Z. Hassan and H. Abu Hassan, Kramers–Kronig analysis of infrared reflectance spectra with a single resonance, *J. Tech.*, 2012, **44**(1), 67–76.
29 L. Janusz, Y. Yi-Hui and C. S. W. Jeffrey, Removal of NOx by Photocatalytic Processes, *J. Photochem. Photobiol., C*, 2013, **14**, 29–52.
30 O. Yoshihisa, N. Yuri, F. Akari, M. Sadao and T. Koji, Photocatalytic Oxidation of Nitrogen Dioxide with TiO2 Thin Films under Continuous UV-Light Illumination, *J. Phys. Chem. C*, 2008, **112**(28), 10502–10508.
31 W. Zheng, S. W. Cao, L. Say Chye Joachim and X. Can, Nanoparticle heterojunctions in ZnS–ZnO hybrid nanowires for visible-light-driven photocatalytic hydrogen generation, *CrystEngComm*, 2013, **15**, 5688–5693.
32 W. Jia, B. Jia, F. Qu and X. Wu, Towards a highly efficient simulated sunlight driven photocatalyst: a case of heterostructured ZnO/ZnS hybrid structure, *Dalton Trans.*, 2013, **42**(39), 14178–14187.
33 L. Dandan, W. Hui, Z. Rui, Z. Wei and P. Wei, Facile Synthesis of Heterostructured ZnO–ZnS Nanocables and Enhanced Photocatalytic Activity, *J. Am. Ceram. Soc.*, 2010, **93**(10), 3384–3389.
34 H. Yong, Q. Huanhuan, L. Yu, D. Gaohui, Z. Fumin, W. Libo and H. Xiao, A microwave-assisted rapid route to synthesize ZnO/ZnS core–shell nanostructures *via* controllable surface sulfidation of ZnO nanorods, *CrystEngComm*, 2011, **13**, 3438–3443.
35 G. Balasubramanian, D. D. Dionysiou, M. T. Suidan, I. Baudin and J. M. Laîné, Evaluating the activities of immobilized TiO2 powder films for the photocatalytic degradation of organic contaminants in water, *Appl. Catal., B*, 2004, **47**, 73–84.